IEEE Access
Multidisciplinary ⋮ Rapid Review ⋮ Open Access Journal

Received December 12, 2019, accepted January 5, 2020, date of publication January 13, 2020, date of current version January 23, 2020.

Digital Object Identifier 10.1109/ACCESS.2020.2966247

Efficient Design of Tightly Coupled Dipole Array Using an Equivalent Circuit-Based Approach

WENYANG ZHOU, YIKAI CHEN, (Senior Member, IEEE), AND SHIWEN YANG, (Fellow, IEEE)
School of Electronic Science and Engineering, University of Electronic Science and Technology of China (UESTC), Chengdu 611731, China

Corresponding author: Yikai Chen (ykchen@uestc.edu.cn)

This work was supported by the Natural Science Foundation of China under Grant 61671127, Grant 61971096, Grant 61631006, and Grant 61721001.

ABSTRACT This paper proposes an efficient and systematic design approach for tightly coupled dipole array (TCDA) designs. In this approach, the radiator structure and feeding structure are designed and optimized based on their equivalent circuit models (ECM) respectively. A novel ECM is proposed to accurately describe the impedance characteristics of the radiator structure with dual-diamond dipoles. The proposed ECM of the radiator structure keeps its accuracy for variable design parameters. The ECM of the proposed feeding structure is also developed to analyze its impedance characteristics. As compared with conventional brute-force optimizations based on full-wave simulations, the two ECMs make it easy and efficient to design wideband TCDAs. A dual-polarized TCDA is designed with the proposed approach to illustrate the efficiency of the approach. The resultant TCDA operates in a wide frequency band of 0.87-10.14 GHz with VSWR$\leq$2 for broadside radiation. Meanwhile, the VSWR value under all conditions (broadside, $\pm 60^\circ$ scanning in E- and H-planes) remains $\leq$3 over the frequency band of 0.8-9 GHz. A 10×10 prototype is fabricated to demonstrate the design.

INDEX TERMS Tightly coupled dipole array (TCDA), equivalent circuit model (ECM), phased array.

I. INTRODUCTION

Performance of wideband phased arrays is always restrained by the contradictory demands for low profile height, ultra-wide bandwidth, and large scanning ranges. In traditional wideband array designs [1], standalone wideband antenna elements should be designed first and mutual coupling should be suppressed in further antenna array development to ensure the bandwidth of the antenna array. The performance of conventional wideband phased array is thus difficult to improve.

Recently, tightly coupled dipole arrays (TCDA) attract growing interests in antenna and propagation community. The most recent work has demonstrated that TCDA is able to achieve 9:1 bandwidth with a wide scanning range of $\pm$ 60° [2]. Similar to connected arrays [3], TCDA [4]–[15] is another practical engineering realizations of Wheeler's theoretical current sheet array concept [1], [16]. In contrast with conventional wideband phased arrays, TCDAs deliberately introduce strong mutual couplings between adjacent antenna elements to extend the bandwidth, rather than suppress the mutual couplings. Specifically, the antenna elements in TCDA are capacitively coupled with each other through overlapped dipole arms, while the antenna elements of connected arrays are directly connected with each other. Actually, capacitive mutual coupling between antenna elements is first introduced in current sheet arrays (CSA) to compensate the inductance from the ground plane [17]. Planar ultrawideband modular antenna (PUMA) [18]–[21] and TCDAs are then proposed to further improve the bandwidth and scanning range of CSA. One of the difficulties in TCDA design is that the performance of an antenna array heavily depends on parameter optimization based on full-wave simulation [10]–[15]. In practice, the parameter optimization is quite time consuming and has become a major obstacle in TCDA design.

To clearly illustrate the proposed approach, we discuss the TCDA design in terms of its radiator structure and feeding structure designs respectively. As shown in Fig. 1, the radiator structure is composed of a superstrate, an antenna plane, a dielectric substrate, a resistive sheet, and a ground plane. The feeding structure consists of a twin slot line and a stripline. Dipole antenna element is the main part

The associate editor coordinating the review of this manuscript and approving it for publication was Kai-Da Xu.

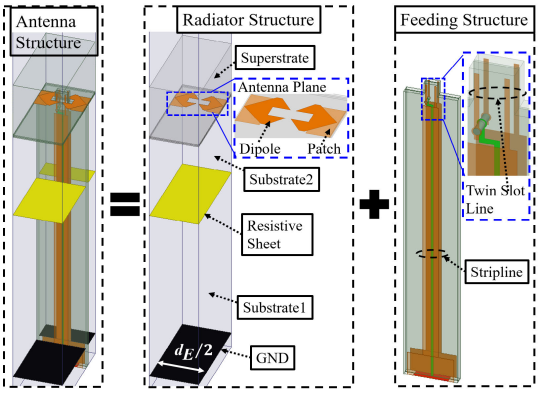

FIGURE 1. The half unit cell of the TCDA. It consists of a radiator structure and a feeding structure.

of the radiator structure of TCDA, thus the first step in TCDA development is to determine the shape of the dipoles. Because of the low- profile height and low cross polarization performance, horizontal bowtie dipoles are widely adopted in TCDA developments [4]–[7]. In dual-polarized TCDA designs, the two orthogonal polarized bowtie dipoles [5]–[7] are usually printed on the two surfaces of a dielectric substrate. Due to the closely spaced antenna elements in TCDAs, such kind of dual-polarized bowtie dipole configuration causes many difficulties in the soldering of feeding structure with the dipole terminals [7]. Alternatively, the PUMA [18] only consists of irregular dipoles over the top surface of dielectric substrate. It indeed facilitates the soldering of dual-polarized antenna array in the assemble stage. However, the equivalent circuit model (ECM) of the irregular dipoles has not been developed in previous research [17], [7]–[9].

It is well known that brute-force optimizations based on full-wave simulations is quite time consuming and usually lack of physical insights. Therefore, the ECM for radiator structure with irregular dipoles is highly demanded. A simple ECM is presented in [17] for the first time to give a physical interpretation of the tightly coupled antenna array. The ECM is then further elaborated to improve its accuracy in characterizing scanning arrays [8]. However, it is time consuming and tedious to extract the equivalent inductance of dipoles when the physical dimensions of the dipoles changes. Thereafter, another improved ECM is proposed in [9] to model the radiator structure with interdigital capacitive couplings [9] and parallel plate capacitive couplings [7]. Furthermore, a mapping relationship between lumped element values and physical dimensions is also developed to speed up the optimization design [9], [7]. However, the ECMs in [7] and [9] are only available for typical dipoles with simple shapes. Alternatively, the ECM is constructed based on Green's function for analyzing the connected arrays [22] and TCDA [23] accurately. Moreover, the size of the rectangular dipole and gap is regarded as variable parameter in the ECM. Nevertheless, the ECMs in [22] and [23] are still only available for standard dipoles. Therefore, it is necessary to develop ECMs for radiator structures with irregular shaped dipoles for achieving high design efficiency and good radiation performances.

In [7], a dual-polarized TCDA working over UHF-X band has been designed. In this paper, we propose an efficient and systematic design approach for TCDA designs. The efficiency and effectiveness of proposed approach is then demonstrated in a new TCDA design. The contributions of the work are summarized as follows,

1) A novel dual-diamond dipole element suitable for dual-polarization and further assembling is proposed.
2) An ECM for analyzing TCDAs' radiator structures with dual-diamond dipoles is developed. The proposed ECM keeps its good accuracy even when the design parameters of the radiator structures are changing.
3) A compact and wideband feeding structure is proposed to excite the radiator structures of the TCDA. The design for the feeding structure is also based on the ECM that we have developed in this work.

The rest of the paper is organized as follows. Section II gives the design procedure for the radiator structure and the novel feeding structure. Section III presents a TCDA designed with the proposed approach. Section IV experimentally validates the performance of the 10×10 dual-polarized TCDA prototype. Conclusions are presented in the Section V.

II. THE PROPOSED DESIGN APPROACH AND ECMS

A. RADIATOR STRUCTURE AND ITS ECM

As was stated previously, the shape of the dipoles has to be determined first in TCDA design. Different from the bowtie dipole, the shape of the end of the proposed dual-diamond dipole is a triangle rather than a rectangle. As shown in Fig. 2(a), the two arms of the dual-diamond dipoles are in diamond shape. Here, the dual-diamond dipole is embedded over the antenna plane of the dual-polarized TCDA. In addition, the dual-polarized antenna element spacing along the E-plane and H-plane is d_E and d_H, respectively. As shown in Fig. 2(a), the antenna plane consists of the dual-diamond dipole and rectangular patches printed on the two surfaces of the dielectric substrate. Moreover, the rectangular patch printed on the bottom surface of the antenna plane overlaps with the dual-diamond dipole arm to form capacitive mutual coupling. As can be seen in Fig. 2(a), the cross point of the two orthogonal polarized dipoles occurs at the dipole end, rather than at the feed. Thus, the triangular shape of the dipole end makes it possible to print the two polarized dipoles on the top surface of the dielectric substrate. Instead, the previous research using standard dipole applies a different dipole configuration for the dual-polarized TCDA. For example, the dipole configuration is that the two polarized dipoles are printed on the two surfaces of the dielectric substrate [5]-[7] in Fig. 2(b). In contrast, it needs to be soldered on both of the two surfaces. Thus, the proposed dual-diamond dipoles will relatively facilitate the feeding point soldering in practical assembling.

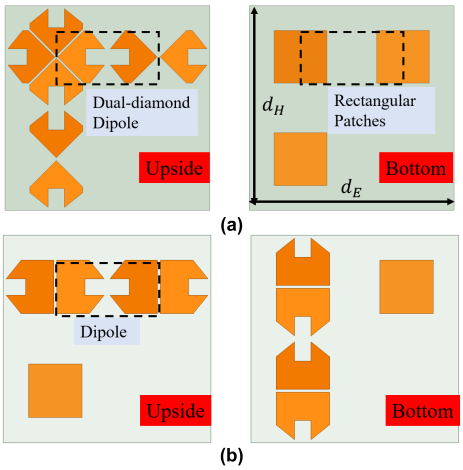

FIGURE 2. The top view of the dual-polarized TCDA using (a) the proposed dual-diamond dipole and rectangular patches; (b) standard dipole [5]–[7].

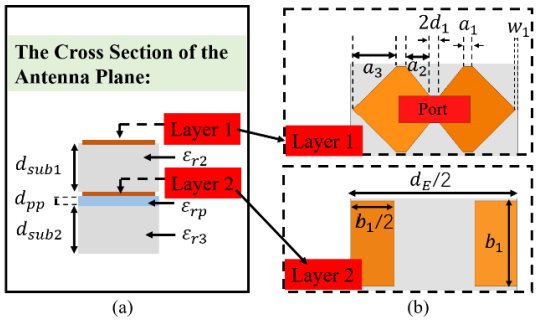

FIGURE 3. Configuration of the antenna plane. (a) The cross section view; (b) the top view.

Next, the size of the dipoles has to be marked by the variable name for the ECM optimization. Fig. 3 shows the configuration of the antenna plane with its dimensions. It consists of three dielectric sheets, and the middle layer (ε_{rp}, d_{pp}) is introduced to glue the three dielectric sheets. The relative permittivity and thickness of the top dielectric sheet and the bottom dielectric sheet are (ε_{r2}, d_{sub1}), and (ε_{r3}, d_{sub2}), respectively. Besides, these parameters are the optimization variables in the ECM. In Fig. 3(b), the dual-diamond dipole and rectangular patches are printed on the upper (Layer 1) and lower (Layer 2) surfaces of the top dielectric sheets, respectively. As can be seen in Fig. 3(b), there is a geometric relationship between the dimensions of the dipole and patches. For example, $b_1 = 2(a_3 + w_1)$ is used to keep the dual-polarized configuration in Fig. 2(a) physically realizable. Moreover, $a_1 + a_2 + a_3 + d_1 + w_1 = d_E/4$ is used to keep the dipole inside the domain of the TCDA period. Then, the TCDA period is a constant value less than half wavelength of the highest frequency in the ECM ($d_E = d_H < \lambda_H/2$). Instead, the dipole size (a_1, a_2, w_1, d_1) are the optimization variables in the ECM. The other design parameters (a_3 and b_1) can be derived by the geometric relationship. In summary, the dipole's optimization variables in the ECM are ε_{r2}, d_{sub1}, ε_{r3}, d_{sub2}, a_1, a_2, w_1, and d_1.

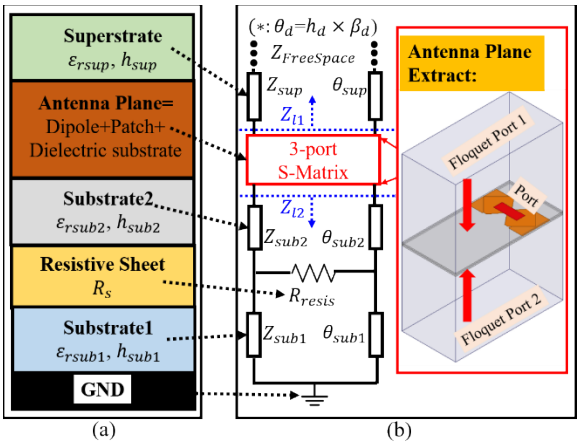

FIGURE 4. The mapping relationship between radiator structure and ECM. (a) The diagram of the radiation structure; (b) The ECM of the radiation structure.

After that, the ECM for analyzing the radiator structure with this kind of dipole has to be developed for efficient optimization design. The conventional ECM [8], [9] does not work out, because it is difficult to find the mapping relationship between the physical dimensions of the proposed dual-diamond dipoles and the lumped element values in circuit model. Fig. 4 gives the conceptual model and the proposed ECM of the radiator structure. As can be seen in Fig. 4(a), each component of the radiator structure could be represented by a parameterized block. Instead of finding the mapping relationship, we directly introduce the three-port S-matrix of the antenna plane into the ECM. The S-Matrix is exported from full-wave simulation through solely simulating the antenna plane with periodic boundary as shown in Fig. 4(b). Then, all of these component blocks can be represented by the circuit components in the ECM. The relative permittivity and thickness of the dielectric superstrate, dielectric substrate 1 and dielectric substrate 2 are (ε_{rsup}, h_{sup}), (ε_{rsub1}, h_{sub1}), and (ε_{rsub2}, h_{sub2}), respectively. These parameters are the optimization variables in the ECM. In addition, the square impedance (R_s) of the resistive sheet is also included as an optimization variable in the ECM. The resistive sheet [4] and dielectric superstrate are used for extending the impedance bandwidth and wide-angle impedance matching (WAIM) [24], [25] respectively. In addition, all the dielectric slabs can be represented by transmission lines (TLs) [26], and the characteristic impedance (Z_d) and electric length (θ_d) relate with the physical parameters (h_d and ε_{rd}) through the following formula,

$$Z_d = \frac{\eta}{\sqrt{\varepsilon_{rd}}} \tag{1}$$

$$\beta_d = k_0\sqrt{\varepsilon_{rd}} \tag{2}$$

$$\theta_d = h_d\beta_d \tag{3}$$

where the subscript d can be replaced with subscript *sup*, *sub1*, and *sub2* to respectively represent the superstrate, dielectric substrate1 and dielectric substrate2. $\eta \approx 377\Omega$ is

the characteristic impedance of free space, and k_0 is the free space wave-number. Then, the resistive sheet is represented by the parallel resistance $R_{resis} = R_s$. The Z_{l1} and Z_{l2} in the ECM are defined as the input impedance looking from the dielectric superstrate TL (Z_{sup}, θ_{sup}) and dielectric substrate 2 TL (Z_{sub2}, θ_{sub2}) along the blue dotted lines shown in Fig. 4(b), respectively. They can be calculated from following equation,

$$Z_{l1} = Z_{\text{sup}} \frac{\eta + jZ_{\text{sup}} \tan\theta_{\text{sup}}}{Z_{\text{sup}} + j\eta \tan\theta_{\text{sup}}} \tag{4a}$$

$$Z_{l2} = Z_{sub2} \frac{Z_{//} + jZ_{sub2} \tan\theta_{sub2}}{Z_{sub2} + jZ_{//} \tan\theta_{sub2}} \tag{4b}$$

where the shunt impedance $Z_{//}$ is given as:

$$Z_{//} = \frac{jR_{resis}Z_{sub1} \tan\theta_{sub1}}{R_{resis} + jZ_{sub1} \tan\theta_{sub1}} \tag{5}$$

As it can be seen in the antenna plane model in Fig. 4(b), the three-port network consists of Floquet Port 1 on the top surface of the air box, Floquet Port 2 on the bottom surface of the air box, and the lumped port for the excitation of the dipole. Finally, the input impedance of the radiator structure is the input impedance of the lumped port in the three-port network when the Floquet Port 1 and Floquet Port 2 are terminated with Z_{l1} and Z_{l2} respectively. In addition, the input impedance of the lumped port can be easily obtained from the approaches in [33].

To illustrate the accuracy of the proposed ECM in terms of many important design parameters, we perform a parameter analysis and compare the resultant VSWR and input impedance with those from full-wave simulations. One part of these design parameters is from the size of dipole. Firstly, we respectively tune the values of the dipole's design parameters a_2 = (0.6mm, 1mm, 1.4mm) and d_{sub1} = (5mil, 10mil, 20mil), meanwhile values of other parameters are fixed ($\varepsilon_{r2} = 10.2$, $\varepsilon_{r3} = 2.2$, $d_{sub2} = 5$mil, $a_1 = 0.4$mm, $w_1 = 0.1$mm, $d_1 = 0.2$mm, $R_s = 120$ Ohms/square, $h_{sub1} = 13$mm, $h_{sup} = 8$mm $\varepsilon_{rsup} = 2.55$, $\varepsilon_{rsub1} = \varepsilon_{rsub2} = 1$, $h_{sub2} = 13$mm). Then, the left panel of Fig. 5 shows the VSWR of the periodic TCDA unit cell obtained from ECM and full-wave simulations for different values of design parameters a_2 and d_{sub1}. As it can be seen, the ECM results in accurate VSWR prediction as compared with full-wave simulation results. After that, the accuracy of the proposed ECM is illustrated through checking the accuracy of the input impedance (real and imaginary) for the design parameters $a_2 = 1$mm, and $d_{sub1} = 10$mil. The comparison results are presented in the right panel of Fig. 5, and it further shows the accuracy of the proposed ECM. Another part of these design parameters is from the resistive sheet and the dielectric sheet. Similarly, we respectively tune the values of these sheets' design parameters R_s = (50 Ohms/square, 200 Ohms/square, 800 Ohms/square), h_{sub1} = (12mm, 14mm, 16mm), and h_{sup} = (4mm, 6mm, 8mm), meanwhile values of other parameters are fixed ($\varepsilon_{r2} = 10.2$, $d_{sub1} = 5$mil $\varepsilon_{r3} = 2.2$, $d_{sub2} = 5$mil, $a_1 = 0.4$mm, $a_2 = 1$mm, $w_1 = 0.1$mm, $d_1 = 0.2$mm, $\varepsilon_{rsup} = 2.55$, $\varepsilon_{rsub1} = \varepsilon_{rsub2} = 1$, $h_{sub2} = 13$mm). Then, the left panel of Fig. 6 shows the VSWR obtained from ECM and full-wave simulations for different values of design parameters R_s, h_{sub1}, and h_{sup}. The right panel of Fig. 6 gives the input impedance (real and imaginary) for the design parameters $R_s = 200$ Ohms/square, $h_{sub1} = 14$mm, and $h_{sup} = 6$mm. It again shows the accuracy of the proposed ECM. Therefore, it is reliable to adopt the proposed ECM for efficient optimization of the radiator structure for achieving wide bandwidth.

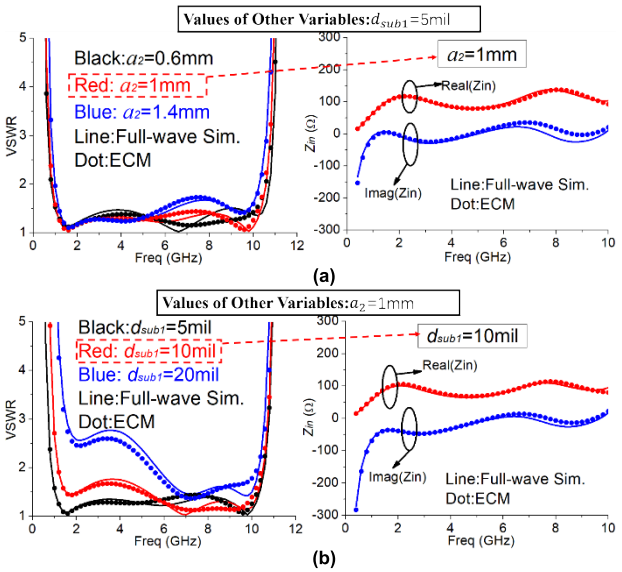

FIGURE 5. Parametric analysis for (a) a_2 and (b) d_{sub1}.

B. FEEDING STRUCTURE AND ITS ECM

Once the radiator stucture has been designed, the feeding structure has to be designed to excite the radiator structure. Similar to the approach introduced in [27], [28], we also analyze the proposed feeding structure using an ECM based on the S-parameters of a two-port network. Fig. 7(a) gives the proposed feeding structure consisting of two kinds of transimission lines, i.e., twin slot line and stripline. The ECM of the feeding structure is shown in Fig. 7(b). Firstly, the twin slot line depicted in Fig. 7(a) can be viewed as two slot lines respectively etched on the two surfaces of a multilayered dielectric sheet. Ground plane of the stripline is printed on the two sides of the multilayered dielectric sheet, and the trace of the stripline is printed on the bottom surface of the top dielectric slab. As it can be seen from Fig. 7(a), the left two PEC strips of the twin slot line connect to the trace of the stripline through a via, and the right two PEC strips are directly connected to the ground plane of the stripline. Moreover, the first segment of the stripline's trace is bent 90° to allow the stripline sitting in the middle of the half unit cell. In addition, the twin slot line also privides the function of transforming the two terminals of the dipole to stripline transimisson line. To analyze the properties of the

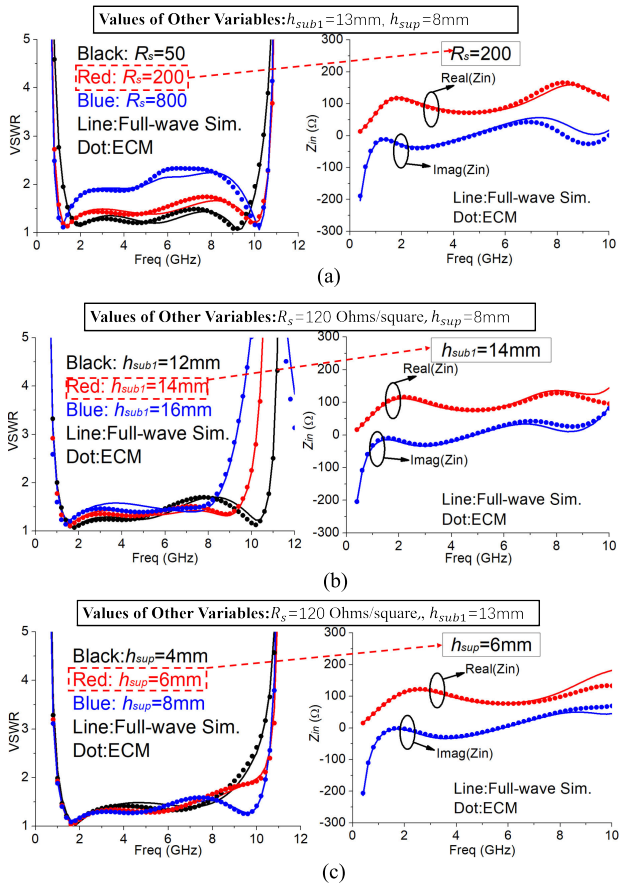

FIGURE 6. Parametric analysis for (a) R_S and (b) h_{sub1}, and (c) h_{sup}.

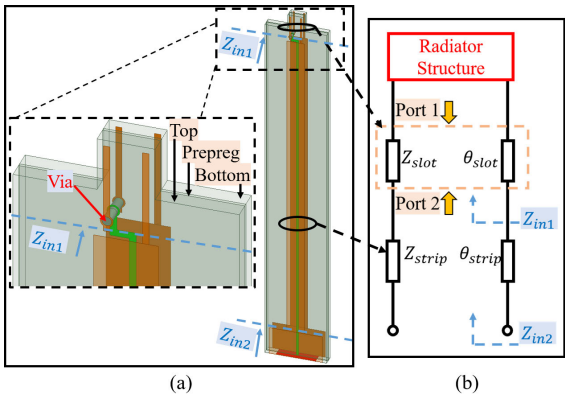

FIGURE 7. The mapping relationship between feeding structure and ECM. (a) The implementation of feeding structure; (b) The ECM of the feeding structure.

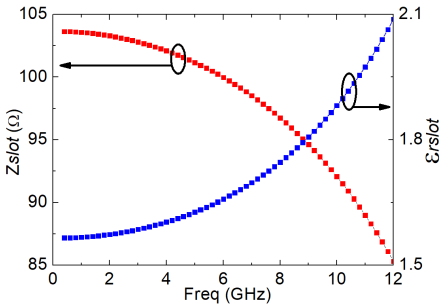

FIGURE 8. The characteristic impedance (Z_{slot}) and relative permittivity (ε_{rslot}) of the twin slot line.

twin slot line, the characteristic impedance (Z_{slot}) and the relative permittivity (ε_{rslot}) of the twin slot line are calculated using the S-parameters extracted from the two-port network of the twin slot lines,

$$\varepsilon_{rslot} = \left(\frac{c \times phase(S_{12})}{2\pi l \times freq}\right)^2 \tag{6}$$

$$Z_{slot} = \sqrt{\frac{imag(B)^2}{1 - real(A)^2}} \tag{7}$$

$$A = \frac{(1 + S_{11})(1 - S_{22}) + S_{12}S_{21}}{2S_{21}} \tag{8a}$$

$$B = Z_0 \frac{(1 + S_{11})(1 + S_{22}) - S_{12}S_{21}}{2S_{21}} \tag{8b}$$

where the operators $phase(\cdot)$, $real(\cdot)$ and $imag(\cdot)$ represent the phase, real part, and imaginary part of the terms in the bracket, respectively. The symbol c is the speed of light, and l is the length of the twin slot line. The symbols A and B are the elements in the transmission matrix of the two-port network [28]. Then, the characteristic impedance (Z_{slot}) and relative permittivity (ε_{rslot}) of the twin slot line is calculated and shown in Fig. 8. As it can be seen, the Z_{slot} and ε_{rslot} does not keep constant over the frequency band. The calculated characteristic impedance is then substituted in the ECM of the feeding structure. Finally, the input impedance (Z_{in1}) looking from the twin slot line at the plane shown in Fig. 7(b) is given by,

$$Z_{in1} = Z_{slot} \frac{Z_r + jZ_{slot} \tan\theta_{slot}}{Z_{slot} + jZ_r \tan\theta_{slot}} \tag{9}$$

where Z_r is the input impedance of the radiator structure. The electrical length (θ_{slot}) of the twin slot line can be calculated by $\theta_{slot} = (2\pi l_3 freq\sqrt{\varepsilon_{rslot}})/c$.

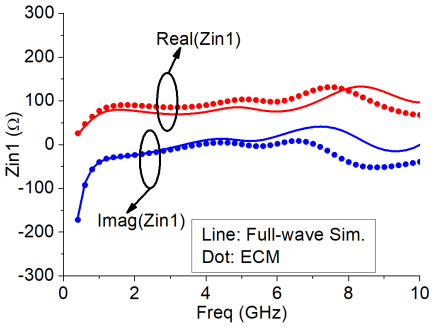

FIGURE 9. The input impedance Z_{in1} calculated by full-wave simulation and ECM.

Fig. 9 compares the input impedance Z_{in1} calculated from full-wave simulation and ECM simulation. The little discrepancy between the full wave simulation and ECM can be seen

at high frequency. It is because that the coupling between the twin slot line and the radiator structure grows up with the increase of frequency. On the other hand, the agreement between ECM results and full-wave simulation results are still acceptable to evaluate the performance of the radiator structure excited by the twin slot line.

III. DUAL-POLARIZED TCDA DEVELOPMENTS

A. TCDA DESIGN WITH ECM

According to the radiator design approach in Section II-A, the period of the TCDA unit cell is first determined to avoid grating lobe ($d_E = d_H = 14$mm). Then we change the values of the dipole's optimization variables, and export the three-port S-matrix of the antenna plane into the ECM. Thus, the S-matrices of the dipole's variables having different value range are already saved in the ECM before optimization. Once S-matrices of the antenna plane have been saved, an ECM was developed using the method in Section II-A for the analysis and optimization of the radiator structure. Fig. 10(a) gives the half unit cell model of the optimized radiator structure. The dielectric substrate 1 and dielectric substrate 2 are air in this design for light weight. Thus, the relative permittivity of them is fixed at $\varepsilon_{r0} = 1$ in optimization ($\varepsilon_{rsub1} = \varepsilon_{rsub2} = \varepsilon_{r0}$). Moreover, the port impedance of the radiator structure is set to 100 Ω for impedance matching. In this design, the design variables ε_{r2}, d_{sub1}, a_1, a_2, w_1, d_1, h_{sup}, h_{sub1}, h_{sub2}, R_s, and ε_{rsup} are optimized by integrating the ECM in a genetic algorithm for objective function evaluation. The optimization procedure is quite efficient as it does not need full-wave simulations. The goal of the optimization is to design a TCDA operating in the frequency band of 0.8-10 GHz with VSWR < 2. Table 1 presents the optimized design variables, and Fig. 10(b) shows the optimized VSWR. It is observed that the optimized design covers the 0.9-11 GHz band with VSWR < 2. In addition, full-wave simulation to the optimized radiator structure is also performed and the VSWR

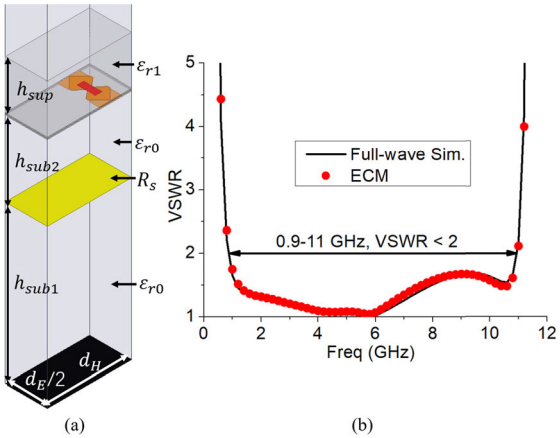

FIGURE 10. Illustration of the optimized radiator structure. (a) The half unit cell model; (b) The simulated VSWR.

TABLE 1. Dimensions of The TCDA.

h_{sup}	h_{sub1}	h_{sub2}	d_{sub1}	d_{sub2}
8 mm	26 mm	12.5 mm	5 mil	5 mil
$(\varepsilon_{r0})^1$	$(\varepsilon_{r1})^2$	$(\varepsilon_{r2})^3$	$(\varepsilon_{r3})^4$	$(\varepsilon_{rp})^5$
(1, 0)	(2.17, 0.0007)	(10.2, 0.0023)	(2.2, 0.0009)	(3.52, 0.0041)
d_{pp}	d_E=d_H	a_1	a_2	a_3
4 mil	14 mm	0.4 mm	1 mm	1.8 mm
d_1	w_1	d_{sub3}	w_2	w_3
0.2 mm	0.1 mm	20 mil	2 mm	0.23 mm
w_4	w_5	w_6	l_1	l_2
0.2 mm	1 mm	1.8 mm	36.9 mm	0.2 mm
l_3	d_2	d_3	d_4	d_5
3.15 mm	0.3 mm	3 mm	1.3 mm	1.2 mm
d_6	d_7	d_8	R_1	R_s
3.25 mm	1 mm	3.3 mm	200 Ω	200 Ohms/square

[1]Air, [2]F_4BMX217, [3]Rogers RT/duroid 6010, [4]Rogers RT/duroid 5880, [5]Rogers RO4450F.

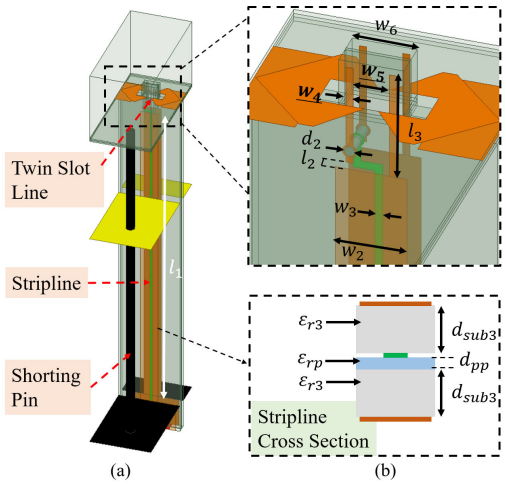

FIGURE 11. Illustration of the designed feeding structure. (a) The half unit cell of the radiator structure excited by the feeding structure; (b) Details of the feeding structure.

is compared with the ECM results. It again demonstrates the accuracy of the proposed ECM.

Based on the design method and the proposed ECM of the feeding structure in Section II-B, the feeding structure is then designed to excite the optimized radiator structure. Fig. 11(a) shows the half unit cell of the radiator structure with the proposed feeding structure. The twin slot line and strapline in the Fig. 11(a) have a characteristic impedance around 100Ω. The dimensions w_2 and w_3 of the 100 Ω stripline can be obtained from the empirical formulas given in [29]. As it can be seen from the cross section of the stripline shown in Fig. 11(b), it consists of a top dielectric sheet (ε_{r3}, d_{sub3}),

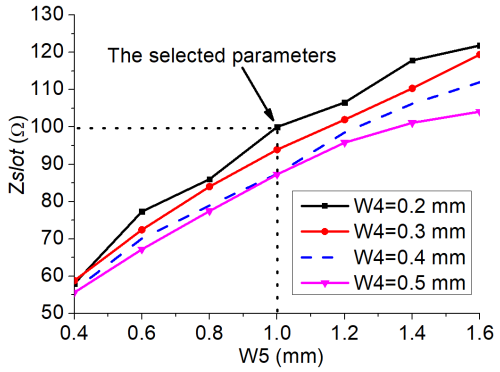

FIGURE 12. The characteristic impedance of the twin slot line at 6 GHz.

a bottom dielectric sheet (ε_{r3}, d_{sub3}), and a layer (ε_{rp}, d_{pp}) for adhesive purpose. Meanwhile, a 100 Ω twin slot line has to be designed for the feeding structure design. Because the dimensions of the multilayered dielectric sheets have been determined in the stripline design, we only need to optimize the design variables w_4 and w_5 for achieving a 100 Ω twin slot line. As can be seen in Fig. 12, the Z_{slot} increases when w_5 increases and w_4 decreases. It is also observed that we can choose $w_4 = 0.2$mm and $w_5 = 1$mm for a 100 Ω twin slot line design.

Once all of the dimensions of the feeding structure are determined, a shorting pin shown in Fig. 11(a) is implemented in the feeding structure to eliminate the common mode resonance in an ultra-wide frequency band. The detailed technique about the common-mode mitigation is provided in [19]. Then, the VSWR of the model with and without shorting pin is given in Fig. 13. As it can be seen, the common mode resonance (red line curve) is indeed caused by the unbalanced feeding and has been successfully eliminated by the shorting pin (blue line VSWR curve). The VSWR corresponding to the input impedance Z_{in2} looking from the stripline in Fig. 7(b) could be calculated from the ECM and is also presented in Fig. 13 for comparison. In the ECM calculation, the characteristic parameters of the stripline are $Z_{strip} = 100.5\Omega$ and $\varepsilon_{rstrip} = 2.455$. Moreover, the length of the stripline is $l_1 = 36.9$ mm. It is shown that a large difference between

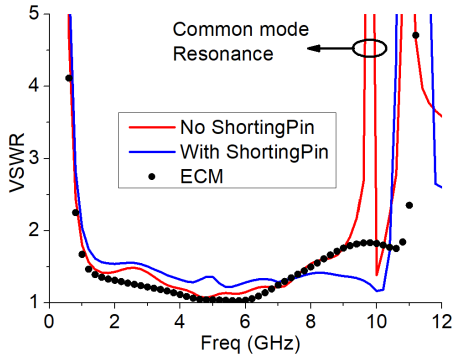

FIGURE 13. The VSWR of various TCDA designs.

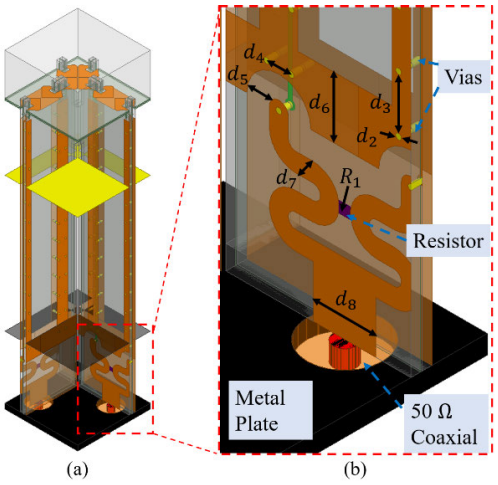

FIGURE 14. Illustration of the dual-polarized TCDA. (a) The unit cell model; (b) Details of the connection between coaxial cable and feeding structures.

ECM and full-wave simulation appears at around 10 GHz. This is caused by the common mode resonance. Because the proposed feeding structure is an unbalanced feed, the net vertical current distribution couples into a resonance that results in a short circuit in the input impedance of the elements [19]. Although, the lumped elements in the proposed ECM of the feeding structure can't illustrate the common mode resonance. The common mode resonance can finally be mitigated by loading shorting pin to basically maintain the ECM's impedance matching performance. In short, the proposed feeding structure and the corresponding ECM based optimization technique could guarantee excellent impedance matching performance over an ultra-wide frequency band. Therefore, the proposed feeding structure is a promising design for ultra-wideband TCDA excitations.

Fig. 14 presents the finalized dual-polarized TCDA. As it can be seen, a via fence is implemented along the stripline to improve the isolation between the two orthogonal polarizations. The two 100 Ω striplines are transformed to two 100 Ω microstrip lines (MSL) through vias and are then parallelly combined to form a single 50 Ω microstrip line. Fig. 15(a) shows the details of the transformation from the stripline to MSL. The gap distance d_5 is critical to the transmission property of the transformation structure. The S-parameters for different d_5 values are shown in Fig. 15(b) to investigate the effect of d_5. The S_{12} remains constant as d_5 varies, but the S_{11} achieves minimum value among 0.4-12 GHz frequency band for $d_5 = 1.2$mm. Therefore, d_5 is selected to be 1.2 mm for the finalized TCDA model. It is also noted that the trace and the ground plane of the MSL are printed on the top and bottom surface of the multilayered dielectric sheets, respectively. It shares the same multilayered dielectric sheet with the twin slot line and the stripline for easy fabrication and assembling. An isolation resistor R_1 is soldered between the two 100Ω MSLs to ensure the scanning performance in

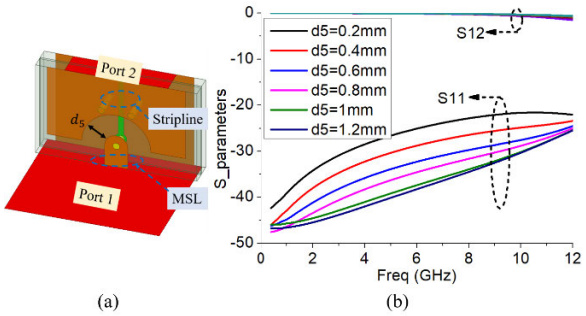

FIGURE 15. The parameter tuning of the transition structure. (a) The transition between stripline and microstrip line; (b) The S-parameters of the transition structure for different d_5 values.

the E-plane. Moreover, a 50 Ω coaxial cable is also introduced to model the practical SMP connector.

B. SIMULATED PERFORMANCE OF THE INFINITE TCDA

The simulated VSWR of the infinite TCDA (TCDA unit cell with periodic boundary) is presented in Fig. 16. As it can be seen, the broadside VSWR is below 2.0 over the frequency band of 0.87-10.14 GHz. In addition, the TCDA achieves ±60° scanning range (VSWR ≤ 3) in the E-plane and H-plane over the frequency band of 0.79-11.76 GHz and 0.73-9.06 GHz, respectively. The relative narrow scanning bandwidth of 60° scanning in the H-plane is caused by a scanning blindness around 10 GHz. The thick superstrate ($\varepsilon_{rsup} = 2.17$, $h_{rsup} = 8$mm) supports surface waves at certain scan angle resulting in scanning blindness [30]. Thus, the superstrate component in the ECM optimization of the radiator structure can be removed if the scanning bandwidth is too narrow to be used in practice.

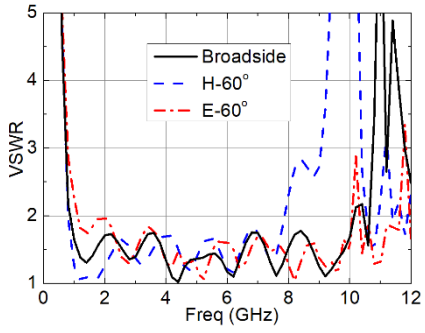

FIGURE 16. The VSWR of the infinite array.

The polarization isolation is shown in Fig. 17. As it can be seen, the S_{12} is below −20 dB for a scanning angle up to 60° in the E- and H-planes. The S_{12} in the diagonal plane (D-plane) arises to around −15 dB for 60° scanning. In addition, we define the cross polarization level of the infinite array as the difference $G_{cross} - G_{co}$ between the co-polarization realized gain G_{co} and cross polarization realized gain G_{cross}. As it can be observed from Fig. 18, the cross polarization level of the TCDA is less than −20 dB when scanning up to 60° in

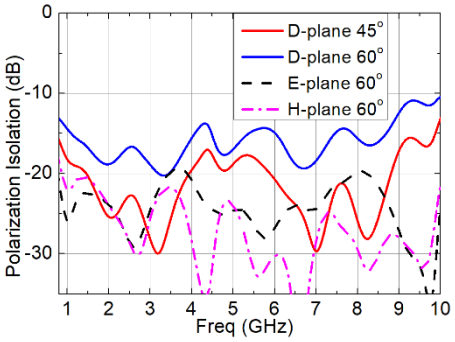

FIGURE 17. The polarization isolation (S_{12}) of the infinite array.

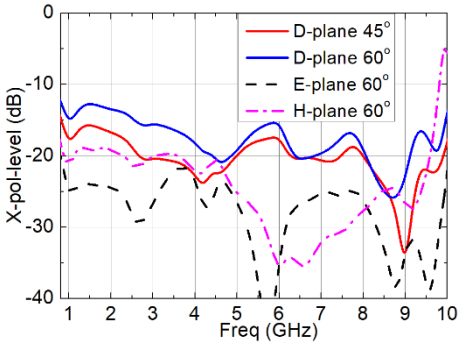

FIGURE 18. The cross-polarization level of the infinite array.

the cardinal planes, and is below ≤ −12 dB and ≤ −15 dB when scanning to 60° and 45° in the D-plane.

IV. EXPERIMENTAL VALIDATIONS

A. PROTOTYPE FABRICATION FOR A 10 × 10 TCDA

Fig. 19 shows the TCDA in different assembling stages. As shown in Fig. 19(a) and (b), the first step is to solder the SMP connectors to the two orthogonal feeding structures for dual-polarizations. The two orthogonal feeding structures are then inserted with each other through the slits on the ground plane and the resistive sheet. The resistive sheet is realized by

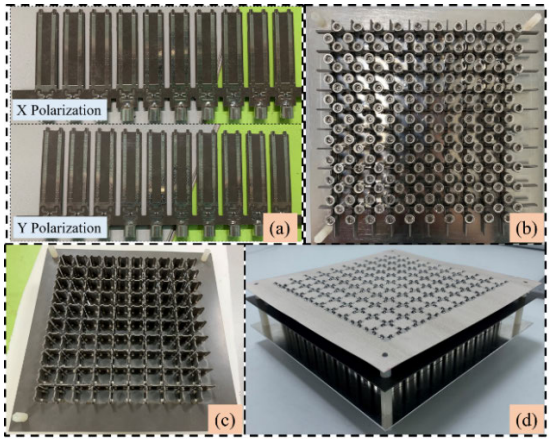

FIGURE 19. The assembling process for the 10×10 prototype.

an indium-tin oxide (ITO) glass glued on a dielectric substrate (Rogers 5880, 20mil). The ITO glasses are connected with the metallic strips of the feeding structures by conductive silver paste (CSP) to obtain desired impedance matching performance for TCDA. Secondly, as shown in Fig. 19(c), the feeding structures are installed over the ground plane of the TCDA. Thirdly, the antenna plane layer is placed over the appropriate position over the feeding structures for soldering. Finally, the superstrate is placed above the antenna plane and then fixed together with the whole structure by the nylon screw. The finalized TCDA prototype with superstrate removed is shown in Fig. 19(d).

B. THE ACTIVE VSWR MEASUREMENT

In order to validate the simulated VSWR of the infinite TCDA, the active VSWR of the center element is investigated. The active reflection coefficient of the center element is calculated through the complex superposition of the center element's S_{11} and the S_{12} between center element and other antenna elements in the array [31]. The scanning angle and antenna element locations have been considered in the active reflection coefficient calculation. The active reflection coefficient is then converted to active VSWR for clear comparison. Fig. 20 shows the measured active VSWR in different scanning conditions. As compared with the simulated VSWR shown in Fig. 16, the agreement between simulated and measured VSWR is reasonable. The slight discrepancy is mainly caused by the difference between the CSP in the fabricated model and the ideal resistive sheet in the simulation model. The fabrication error and the assemble error also contributes to the discrepancy.

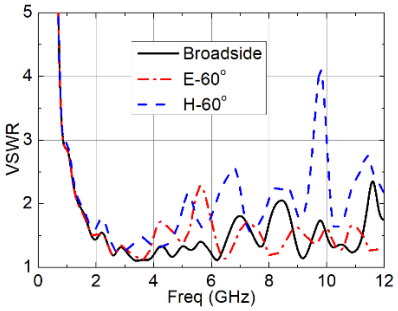

FIGURE 20. The measured active VSWR of the center element in TCDA.

C. MEASURED RADIATION PATTERNS

The measured radiation pattern of the 10 × 10 TCDA is obtained by combining each element's measured unit-excitation active element pattern (UEAEP) [32]. The scanning angle and antenna element locations were also considered in the post-processing based on each UEAEP. Fig. 21 shows measured realized gain of the 10 × 10 TCDA. Simulated realized gain is also presented in Fig. 21 for comparison. The measured results well demonstrate the effectiveness of the TCDA designs. The measured cross-polarization level is also below −20 dB. In addition, the

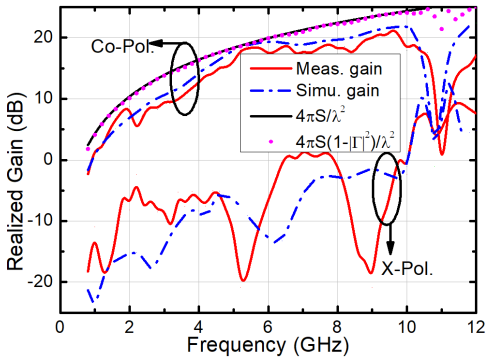

FIGURE 21. The measured and simulated realized gain.

ideal gain of the antenna array calculated from $4\pi S/\lambda^2$ is also shown in Fig. 21, where S is the radiation aperture of the 10 ×10 TCDA array. Moreover, the mismatched gain $(4\pi S(1-|\Gamma|^2)/\lambda^2)$ considering the reflection coefficient (Γ) at each port is also presented in Fig. 21. As it can be seen, the mismatched gain agrees well with the ideal gain. It indicates that the gain loss caused by the impedance mismatch is very low.

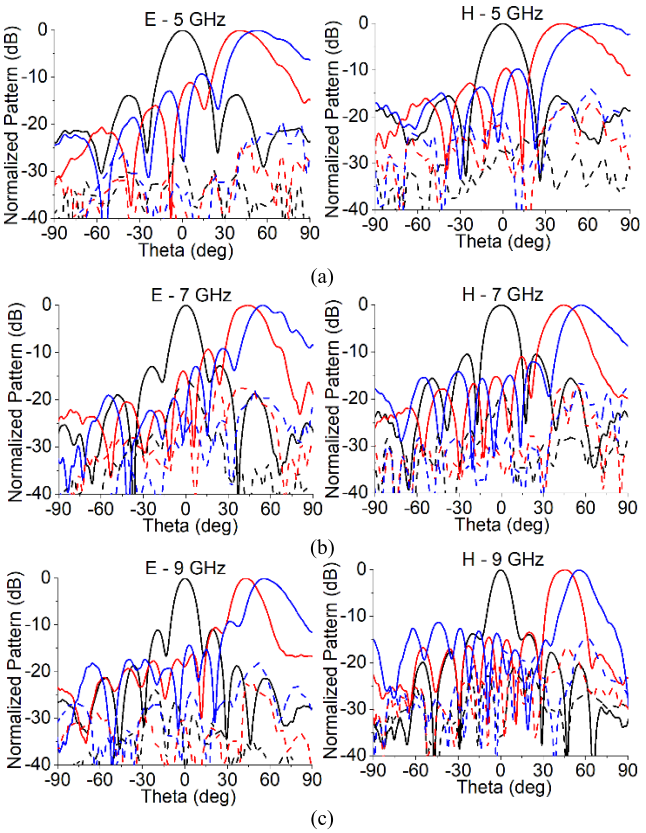

FIGURE 22. The normalized radiation patterns of the 10 × 10 TCDA prototype when scanning to 0° (black line), 45° (red line) and 60° (blue line) in E-plane (left) and H-plane (right) at (a) 5 GHz; (b) 7 GHz; (c) 9 GHz.

Fig. 22 shows the scanning radiation pattern of the 10 × 10 prototype at typical frequencies in the E- and H-planes,

respectively. The little ripples in some of the radiation patterns are caused by the measurement errors. As it was shown in Fig. 22, the radiation beam of the TCDA is able to steer to a desired angle precisely across a wide frequency band in a scanning range of ±60° in the E- and H-planes. In addition, the side lobe level is less than −10 dB and the cross-polarization level keeps below −20dB under all scanning conditions.

V. CONCLUSION

This paper presents a novel approach for the efficient design of TCDA. ECMs for radiation structures and feeding structures are developed for efficient and accurate optimization design. Parametric analysis is performed to show the accuracy of the ECM for different design variables. In addition, as compared with conventional dipoles in TCDAs, the proposed dual-diamond dipole makes it much easier in antenna array assembling. A novel feeding structure is also developed to ensure stable impedance matching across an ultra-wide frequency band. The TCDA developed in this work covers the frequency band of 0.87-10.14 GHz for broadside radiation. It also achieves a scanning range of ±60° in the E- and H-planes. A 10 × 10 prototype is fabricated and measured to validate the design.

REFERENCES

[1] W. F. Croswell, T. Durham, M. Jones, D. Schaubert, P. Friederich, and J. G. Maloney, "Wideband arrays," *Modern Antenna Handbook*. Hoboken, NJ, USA: Wiley, 2008, pp. 581–629.
[2] J. Zhong, A. Johnson, and E. A. Alwan, "Dual-linear polarized phased array with 9:1 Bandwidth and 60° scanning off broadside," *IEEE Trans. Antennas Propag.*, vol. 67, no. 7, pp. 1996–2001, Mar. 2019.
[3] R. Hansen, "Linear connected arrays," *IEEE Antennas Wireless Propag. Lett.*, vol. 3, no. 1, pp. 154–156, Dec. 2004.
[4] W. F. Moulder, K. Sertel, and J. L. Volakis, "Ultrawideband superstrate-enhanced substrate-loaded array with integrated feed," *IEEE Trans. Antennas Propag.*, vol. 61, no. 11, pp. 5802–5807, Nov. 2013.
[5] M. H. Novak and J. L. Volakis, "Ultrawideband antennas for multiband satellite communications at UHF-Ku frequencies," *IEEE Trans. Antennas Propag.*, vol. 63, no. 4, pp. 1334–1341, Jan. 2015.
[6] D. K. Papantonis and J. L. Volakis, "Dual-polarized tightly coupled array with substrate loading," *IEEE Antennas Wireless Propag. Lett.*, vol. 15, pp. 325–328, 2016.
[7] W. Zhou, Y. Chen, and S. Yang, "Dual-polarized tightly coupled dipole array for UHF-X-band satellite applications," *IEEE Antennas Wireless Propag. Lett.*, vol. 18, no. 3, pp. 467–471, Jan. 2019.
[8] J. P. Doane, K. Sertel, and J. L. Volakis, "A wideband, wide scanning tightly coupled dipole array with integrated balun (TCDA-IB)," *IEEE Trans. Antennas Propag.*, vol. 61, no. 9, pp. 4538–4548, Sep. 2013.
[9] B. Riviere, H. Jeuland, and S. Bolioli, "New equivalent circuit model for a broadband optimization of dipole arrays," *IEEE Antennas Wireless Propag. Lett.*, vol. 13, pp. 1300–1304, 2014.
[10] Y. Chen, S. Yang, and Z. Nie, "The role of ground plane plays in wideband phased array antenna," in *Proc. IEEE Int. Conf. Ultra-Wideband (ICUWB)*, vol. 2, Sep. 2010, pp. 829–831.
[11] Y. Chen, S. Yang, and Z. Nie, "A novel wideband antenna array with tightly coupled octagonal ring elements," *Prog. Electromagn. Res.*, vol. 124, pp. 55–70, Jan. 2012.
[12] H. Zhang, S. Yang, Y. Chen, J. Guo, and Z. Nie, "Wideband dual-polarized linear array of tightly coupled elements," *IEEE Trans. Antennas Propag.*, vol. 66, no. 1, pp. 476–480, Jan. 2018.
[13] H. Zhang, S. Yang, S. Xiao, Y. Chen, and S. Qu, "Low-profile, lightweight, ultra-wideband tightly coupled dipole arrays loaded with split rings," *IEEE Trans. Antennas Propag.*, vol. 67, no. 6, pp. 4257–4262, Jun. 2019.
[14] H. Zhang, S. Yang, S.-W. Xiao, Y. Chen, S.-W. Qu, and J. Hu, "Ultrawideband phased antenna arrays based on tightly coupled open folded dipoles," *IEEE Antennas Wireless Propag. Lett.*, vol. 18, no. 2, pp. 378–382, Feb. 2019.
[15] A. O. Bah, P.-Y. Qin, R. W. Ziolkowski, Y. J. Guo, and T. S. Bird, "A wideband low-profile tightly coupled antenna array with a very high figure of merit," *IEEE Trans. Antennas Propag.*, vol. 67, no. 4, pp. 2332–2343, Apr. 2019.
[16] H. Wheeler, "Simple relations derived fom a phased-array antenna made of an infinite current sheet," *IEEE Trans. Antennas Propag.*, vol. 13, no. 4, pp. 506–514, Jul. 1965.
[17] B. A. Munk, "Broadband wire arrays," in *Finite Antenna Arrays and FSS*. Hoboken, NJ, USA: Wiley, 2003.
[18] J. T. Logan, R. W. Kindt, M. Y. Lee, and M. N. Vouvakis, "A new class of planar ultrawideband modular antenna arrays with improved bandwidth," *IEEE Trans. Antennas Propag.*, vol. 66, no. 2, pp. 692–701, Feb. 2018.
[19] S. S. Holland and M. N. Vouvakis, "The planar ultrawideband modular antenna (PUMA) array," *IEEE Trans. Antennas Propag.*, vol. 60, no. 1, pp. 130–140, Jan. 2012.
[20] M. Y. Lee, J. T. Logan, R. W. Kindt, and M. N. Vouvakis, "Simplified design of 6:1 PUMA arrays," in *Proc. IEEE Int. Symp. Antennas Propag. USNC/URSI Nat. Radio Sci. Meeting*, Jul. 2015, pp. 2515–2516.
[21] S. S. Holland, D. H. Schaubert, and M. N. Vouvakis, "A 7–21 GHz dual-polarized planar ultrawideband modular antenna (PUMA) array," *IEEE Trans. Antennas Propag.*, vol. 60, no. 10, pp. 4589–4600, Oct. 2012.
[22] D. Cavallo, A. Neto, and G. Gerini, "Green's function based equivalent circuit for connected arrays in transmission and in reception," *IEEE Trans. Antennas Propag.*, vol. 59, no. 5, pp. 1535–1545, May 2011.
[23] D. Cavallo, A. Neto, and G. Gerini, "Analytical description and design of printed dipole arrays for wideband wide-scan applications," *IEEE Trans. Antennas Propag.*, vol. 60, no. 12, pp. 6027–6031, Dec. 2012.
[24] S. Lee and R. Mittra, "Radiation from dielectric-loaded arrays of parallel-plate waveguides," *IEEE Trans. Antennas Propag.*, vol. 16, no. 5, pp. 513–519, Sep. 1968.
[25] E. Magill and H. Wheeler, "Wide-angle impedance matching of a planar array antenna by a dielectric sheet," *IEEE Trans. Antennas Propag.*, vol. 14, no. 1, pp. 49–53, Jan. 1966.
[26] A. K. Bhattacharyya, *Phased Array Antennas: Floquet Analysis, Synthesis, BFNs and Active Array System*. Hoboken, NJ, USA: Wiley, 2006.
[27] R. Lin Li, T. Wu, B. Pan, K. Lim, J. Laskar, and M. Tentzeris, "Equivalent-circuit analysis of a broadband printed dipole with adjusted integrated balun and an array for base station applications," *IEEE Trans. Antennas Propag.*, vol. 57, no. 7, pp. 2180–2184, Jul. 2009.
[28] D. M. Pozar, *Microwave Engineering*. Hoboken, NJ, USA: Wiley, 2009.
[29] H. Wheeler, "Transmission-line properties of a strip line between parallel planes," *IEEE Trans. Microw. Theory Techn.*, vol. MTT-26, no. 11, pp. 866–876, Nov. 1978.
[30] D. Pozar and D. Schaubert, "Scan blindness in infinite phased arrays of printed dipoles," *IEEE Trans. Antennas Propag.*, vol. 32, no. 6, pp. 602–610, Jun. 1984.
[31] R. C. Hansen, *Phased Array Antennas*. Hoboken, NJ, USA: Wiley, 2009.
[32] D. M. Pozar, "The active element pattern," *IEEE Trans. Antennas Propag.*, vol. 42, no. 8, pp. 1176–1178, Aug. 1994.
[33] J. X. Yun and R. G. Vaughan, "A view of the input reflection coefficient of the n-port network model for MIMO antennas," in *Proc. IEEE Int. Symp. Antennas Propag. (APSURSI)*, Jul. 2011, pp. 297–300.

WENYANG ZHOU was born in Panzhihua, Sichuan, China, in 1994. He received the B.Sc. degree in electromagnetics and wireless technology from the University of Electronic Science and Technology of China (UESTC), Chengdu, China, in 2015, where he is currently pursuing the Ph.D. degree in electromagnetics and microwave technology.

His current research interests include UWB antenna arrays, phased arrays, and low-scattering antennas and arrays.

YIKAI CHEN (Senior Member, IEEE) was born in Hangzhou, China, in 1984. He received the B.Eng. and Ph.D. degrees in electromagnetics and microwave technology from the University of Electronic Science and Technology of China (UESTC), Chengdu, China, in 2006 and 2011, respectively.

From 2011 to 2015, he was a Research Scientist with the Temasek Laboratories, National University of Singapore, Singapore. In 2015, he joined UESTC, as a Full Professor. He has authored or coauthored over 130 peer-reviewed articles and 34 patents/patent disclosures. He has coauthored the book entitled *Characteristic Modes: Theory and Applications in Antenna Engineering* (John Wiley, 2015) and one book chapter to *Differential Evolution: Fundamentals and Applications in Electrical Engineering* (IEEE Wiley, 2009). His current research interests include antenna engineering, computational electromagnetics, and evolutionary optimization algorithms in electromagnetic engineering.

Dr. Chen is also a member of the Applied Computational Electromagnetics Society (ACES). He was a recipient of the National Excellent Doctoral Dissertation Award of China, in 2013. He was recognized as the Hundred Talents Program Professor of the UESTC, the Thousand Talents Program Professor of China, and the Thousand Talents Program Professor of Sichuan Province, China, in 2015, 2016, and 2017, respectively. He serves as the Associate Editor of the *Electronics Letters* and the *Chinese Journal of Electronics*, the review boards of 11 journals, and has also served many international conferences as a TPC Member, a Session Organizer, and a Session Chair.

SHIWEN YANG (Fellow, IEEE) was born in Langzhong, Sichuan, China, in 1967. He received the B.S. degree in electronic science and technology from East China Normal University, Shanghai, China, in 1989, and the M.S. degree in electromagnetics and microwave technology and the Ph.D. degree in physical electronics from the University of Electronic Science and Technology of China (UESTC), Chengdu, China, in 1992 and 1998, respectively.

From 1994 to 1998, he was a Lecturer with the Institute of High Energy Electronics, UESTC. From 1998 to 2001, he was a Research Fellow with the School of Electrical and Electronic Engineering, Nanyang Technological University, Singapore. From 2002 to 2005, he was a Research Scientist with the Temasek Laboratories, National University of Singapore, Singapore. Since 2005, he has been a Full Professor with the School of Electronic Engineering, UESTC. Since 2015, he has been the Chang-Jiang Professor nominated by the Ministry of Education of China. He has authored or coauthored over 300 technical articles. His current research interests include antennas, antennas arrays, optimization techniques, and computational electromagnetics.

Dr. Yang was a recipient of the Foundation for China Distinguished Young Investigator presented by the National Natural Science Foundation of China, in 2011. He is also the Chair of the IEEE Chengdu AP/EMC Joint Chapter. He serves as the Editorial Board Member of the *International Journal of Antennas and Propagation* and *Chinese Journal of Electronics*.